Фізика аеродисперсних систем. – 2022. – № 60. – С.120-142

ЕЛЕКТРОФІЗИКА

UDC 621.791; 533.9

Vishnyakov V.I.[1,2]***, Darakov D.S.***[2]***, Ennan A.A.*** [1]***, Kiro S.A.***[1]

[1] *Physical-Chemical Institute for Environment and Human Protection, 3 Preobrazhenska st., Odessa UA-65082, Ukraine*

[2] *Odesa I. I. Mechnikov National University, 2 Dvoryanska st., Odessa UA-65082, Ukraine*

Fume emissions by electric arc during gas metal arc welding

The influence of welding arc regime on the welding fumes formation is studied by numerical modeling via description of separate processes inside the space charge regions near electrodes in the welding arc with consumable electrode. The modeling comprises the calculation of temperature profiles for electrons and heavy component, calculation of space distribution of gas components' number densities, of gas particles' mean free pathes, of electric potential and field, calculation of the heat transfer from electrode wire (anode) to molten pool (cathode). The formation of high temperature metal vapor from molten pool to environment as a function of arc current is demonstrated. The nucleation in the plasma of welding fumes is considered with taken into account ionization of vapor atoms via their interaction with nucleus surface. The growth of nucleus droplets via vapor condensation and coalescence is calculated. The coagulation of solid primary particles for various values of welding current is calculated and inhalable particle size distribution is demonstrated.

Keywords: Welding arc, Plasma, Metal vapor, Condensation, Coagulation

1. Introduction. The arc welding is based on the electric discharge in gas with high amperage, which is called an electric arc. Electric arc causes ionization of the gas atoms and forms the plasma with temperature about 10000-20000 K, which allows to use the electric arc for melting and welding of metals.

The arc column is surrounded by shielding gas, which protects the molten metal in droplets and weld pool from oxidation. The shielding gas is evaporated from electrode covering in shield metal arc welding (SMAW) or is injected into welding workspace in gas metal arc welding (GMAW) and gas tungsten arc welding (GTAW), which are different by type of electrodes. The consumable or non-consumable electrodes can be used in arc welding with shielding gas. In the first case (GMAW), there is a melting of welding wire and transfer of metal droplets to weld pool, where the weld joint is formed. In the second case (GTAW), the electrode is used only for arc providing, and the welding wire is entered directly into the weld pool.

Arc welding create the serious ecology dangers, because it is the source of welding fumes, which are formed via metal vapors condensation, and has toxically hazard for human and environment. The study of these dangers and their minimization are the important problem, as the arc welding is used very widely.

The experimental studies of electric arc in the welding process are complicated because arc column is not stable, but continuously moves on the welded surface. The optical or probe techniques are inapplicable in these conditions. Only high-speed

DOI: 10.18524/0367-1631.2022.60.267071

photography in the visible and infrared ranges allows to record the droplets transfer and temperature distribution in arc.

Therefore, search of the welding arc authentic computer model is the important problem. Many authors calculate the arc plasma parameters via numerical solving of the classical equations system [1-8]. It is difficult to understand at such approach, how this or that process influence the arc parameters and welding fume properties.

The simplified sequential modeling of separate processes in boundary layers of plasma near anode and cathode is proposed in the present paper. Thus, modeling comes down to the solution of separate tasks, such as space distribution of temperature or particle number densities, in the anode and cathode regions. These tasks are united in the common problem, as processes influence at each other, which is solved by approximation method. The purpose of modeling is determination of vapor formation rate, which is flowed out from molten pool to environment, because this metal vapor is the source of welding fumes.

The temperature of welding wire tip is about of boiling temperature, when arc welding with consumable electrode is used. Therefore, metal vapor forms the layer near electrode tip surface with high number of the iron atoms [9], which provide the electron and ion number densities via thermal ionization. These free charge carriers provide the space charge regions near anode and cathode, which determine the electric current through arc. The space charge region is the main research object in the presented modeling.

The high-temperature metal vapor from arc mixes with the shielding gas and cools. At some temperature the vapor supersaturation reaches critical value, which provides the nucleation beginning. The heterogeneous ion-induced nucleation occurs, because vapor-gas mixture is ionized. The presented consideration of nucleation is took into account the exchange of charges and energy between ionized environment and nuclei. The droplets of nuclei grow via vapor condensation and coalescence up to solidification. Then coagulation of solid primary particles occurs. These processes are considered in the present paper for various values of welding current.

The consideration is focused on conditions of our experiments [10, 11]: reverse polarity, when electrode wire is positive (anode) and the molten pool is negative (cathode); welding wire with 0.8 mm diameter; arc voltage of 18 to 30 V; arc current of 50 to 150 A; wire feed speed of 4 to 12 cm/s; shielding gas flow rate of 6 to 12 lpm. The plasma outside near-electrode layer is considered in the local thermodynamic equilibrium (LTE) with temperature $T_{pl} = 15000$ K, for definiteness [6].

2. Modeling of welding arc.

2.1. Temperature space distribution. The traditional description of arc plasma adjacent to anode surface is based on division of the near-anode layer into several zone [8, 12], such as sheath, presheath and arc column. The sheath zone is a space charge layer, where the plasma neutrality is disturbed and the potential drop between plasma and anode is formed.

The mean free path of iron atoms near consumable electrode (which is anode, when reverse polarity is used) with temperature $T_w \sim 3000$K is described by the following expression [8]:

$$\lambda_a = \frac{1}{n_{aw} Q_a} \sim 1 \mu m, \tag{1}$$

where $Q_a = 4\pi r_a^2$ is the atom collision cross section; r_a is the atom radius; $n_{aw} = p_{sat} / k_B T_w$ is the atom number density near electrode tip surface; k_B is the Boltzmann constant; p_{sat} is the saturated vapor pressure over electrode surface, $\log_{10}(p_{sat}) = A - B / T_w$, A and B is the Antoine constants for iron vapor.

The Eq. (1) is defined the Knudsen layer with collisionless plasma near anode tip surface. In the Langmuir sheath model [13] is noted that description of heat transfer from the plasma to the electrode using plasma thermal conductivities cannot be used in collisionless layer. Instead, heat transfer from the plasma to the electrode is determined by the charged particle fluxes through the layer.

The presheath zone is the region of non-isothermal quasineutral plasma, where the electrons and ions are generated via thermal ionization [12]. This consideration assumes that Debye screening length r_D is essentially smaller than the mean free path Eq. (1). However, the metal vapor from consumable anode influences the physical properties of arc plasma and, consequently, the processes of mass, energy and charge transfer [7, 14].

In this case, as it demonstrated below (Fig. 3), screening length near anode also $r_D \sim 1 \mu m$. Therefore, near-anode layer cannot be divided into sheath and presheath in this case, and for atoms, which are evaporated from electrode, Fourier's law with Newton's law of cooling can be used and allow defining the temperature gradient near electrode surface [15]:

$$\frac{dT}{dz} = \frac{h_c}{k}\left(T_{pl} - T\right), \tag{2}$$

where h_c is the heat transfer coefficient, k is the thermal conductivity, z is the coordinate directed from welding wire to molten pool, and radiation loss is neglected.

The heat transfer coefficient for wire electrode $h_c \sim 3 \mathrm{kWm}^{-2} K^{-1}$ [16], and thermal conductivity is

$$k(T) = \frac{1}{3} \rho c_p \lambda_a v_{Ta} = \frac{m_a c_p v_{Ta}(T)}{3 Q_a}, \tag{3}$$

where $\rho = n_a m_a$ is the mass density; m_a is the iron atom mass; $c_p = 5R/2\mu$ is the isobaric heat capacity; μ is the iron molecular weight; $v_{Ta}(T) = \sqrt{8 k_B T / \pi m_a}$ is the atom thermal velocity, R is the ideal gas constant.

Thus, it is possible to defined the characteristic length for Eq. (2) as

$$l = \frac{k}{h_c} = l_{pl} \sqrt{\frac{T_{pl}}{T}}.$$

where $l_{pl} = m_a c_p v_{Ta}(T_{pl}) / 3 \mathrm{Q}_a h_c$ (in the system under consideration $l_{pl} \cong 15 \mu m$). Accordingly, Eq. (2) can be presented in the following form

$$\frac{dT}{dz} = \frac{T_{pl} - T}{l_{pl}} \sqrt{\frac{T_{pl}}{T}}. \tag{4}$$

This equation has cumbersome solution that, however, can be approximated by function

$$T_h(z) = \left(T_{pl}^{1.8} - \left(T_{pl}^{1.8} - T_w^{1.8} \right) \exp\frac{-z}{l_{pl}} \right)^{\frac{1}{1.8}}, \qquad (5)$$

which is presented in Fig. 1 together with solution of Eq. (4). The electrode tip temperature is T_w = 3000 K; the temperature in arc region is T_{pl} = 15000 K. The definition T_h is used for heavy component (ions and atoms).

2.2. Space distributions of gas particles. The vapor mass flow from consumable electrode wire is $J_{0Fe} = A_w j_{0Fe}$, where

$$j_{0Fe} = p_{sat}\sqrt{\frac{\mu}{2\pi R T_w}}, \qquad (6)$$

is the iron vapour mass flux from electrode in the Hertz-Knudsen-Langmuir approximation [17] and Aw is the tip surface area.

This flow is mixed with shielding gas mass flow J_{sg}: $J_{mix} = J_{0Fe} + J_{sg}$. The mixture flow divergence along coordinate z in the linear approach is

$$\frac{dJ_{mix}}{dz} = \frac{J_{mix}}{z_0}, \qquad (7)$$

where z_0 is the mixing length, which is defined as $z_0 = kd_w$; d_w is the welding wire diameter; $k = 0.4$ is the Karman-Prandtl constant [18].

From Eq. (7) follows $J_{mix} = J_{0Fe} exp\left(z / z_0\right)$ and $J_{sg} = J_{0Fe}\left(exp\left(z / z_0\right) - 1\right)$.

The conservation of iron mass requires $g_{Fe} J_{mix} = J_{0Fe}$, where g is the component mass fraction. Hence,

$$g_{Fe}(z) = exp\left(-z / z_0\right), \quad g_{sg}(z) = 1 - \exp\left(-z / z_0\right) \qquad (8)$$

The analysis of the experimental data [19] demonstrates that distribution of ratio g_{Fe}/g_{sg} along coordinate z is described well by Eq. (8), which allows to calculate the available for ionization atom number density

$$n_{Aj}(z) = \frac{g_j(z) p_{atm}}{k_B T_h(z)}, \qquad (9)$$

where p_{atm} is the atmospheric pressure.

The atom ionization in the arc column occurs via electron-atom collisions and via photoionization by UV radiation. However, photoionization performs weak effect on the ionization balance [20], which, therefore, can be determined by Saha equation [21]

$$\frac{n_e n_i}{n_a} = \frac{\Sigma_i}{\Sigma_a} v_e(T) \exp\left(-\frac{E_{ion}}{k_B T} \right) \equiv K_S(T), \qquad (10)$$

where n_e, n_i and n_a are the average number densities of electrons, ions and atoms, respectively; $n_a = n_A - n_i$; Σ_i and Σ_a are the ion and atom statistical weights; $v_e(T) =$

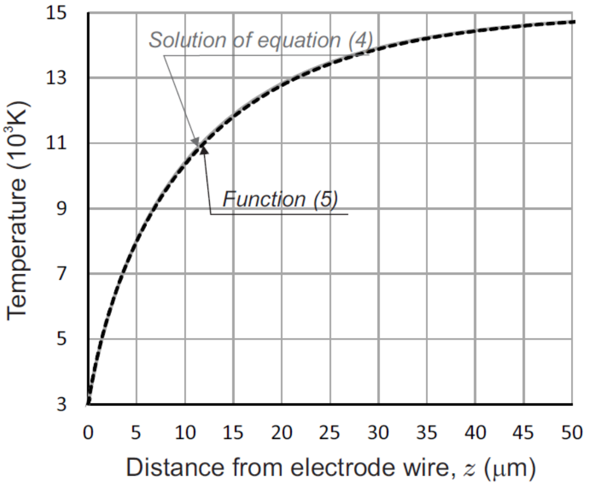

Fig. 1: Heavy component temperature space distribution in electrode layer: grey solid curve is the solution of Eq. (4); black dashed curve is the function Eq. (5).

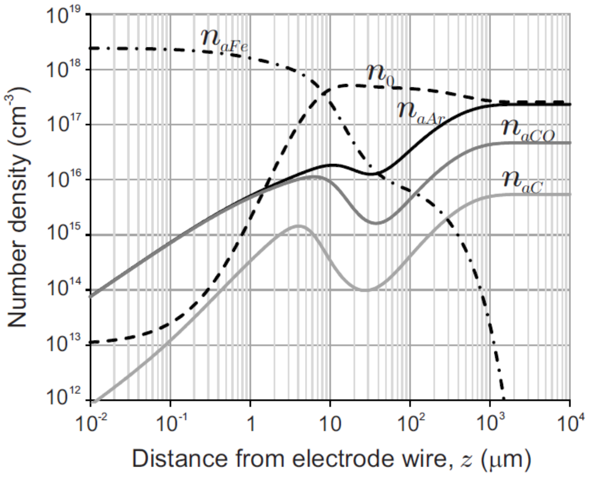

Fig 2: Space distributions of unperturbed number density $n0$, atom number density for iron n_{aFe} for two kinds of shielding gas: pure argon (n_{aAr}) and pure carbon dioxide (n_{aC} and n_{aCO}).

$2\left(m_e k_B T / 2\pi\hbar^2\right)^{3/2}$ is the effective density of the electron states; E_{ion} is the atom ionization energy; $\hbar$ is the Plank constant; K_S is the Saha constant.

In the unperturbed plasma the neutrality condition $n_e = n_i = n_0$ is valid, where n_0 is the unperturbed number density, which value follows from Saha equation for each component:

$$n_{0j}(z)=\frac{K_{Sj}(T_h(z))}{2}\left(\sqrt{1+4\frac{n_{Aj}(z)}{K_{Sj}(T_h(z))}}-1\right), \qquad n_0(z)=\sum_j n_{0j},$$

and atom number density for each component is

$$n_{aj}(z) = n_{Aj}(z)-n_{0j}(z). \tag{11}$$

The space distribution of the unperturbed number density $n0(z)$ is presented in Fig. 2. Distributions of the iron atoms' number density and the number density of shielding gas atoms are also presented for two types of shielding gas: argon and carbon dioxide. The carbon dioxide is dissociated in the arc plasma to CO, O and C; however, CO2, CO and O have ionization potential about 14 eV. Carbon ionization potential is 11.3 eV. Therefore CO2, CO and O atoms are combined in n_{aCO}. The temperature dependency of carbon dioxide decomposition $g_{j0}(T)$ from [22] was used. Almost all iron atoms are ionized at the distance from anode more than 1 mm, because they have lowermost ionization potential (7.9 eV) in this system.

2.3. Mean free paths of gas particles. Mean free path of the particle is defined by its thermal velocity $v_T = \sqrt{8k_B T / \pi m}$ and collision frequency with target particles f: $\lambda = v_T / f$ [23].

The collision frequency is

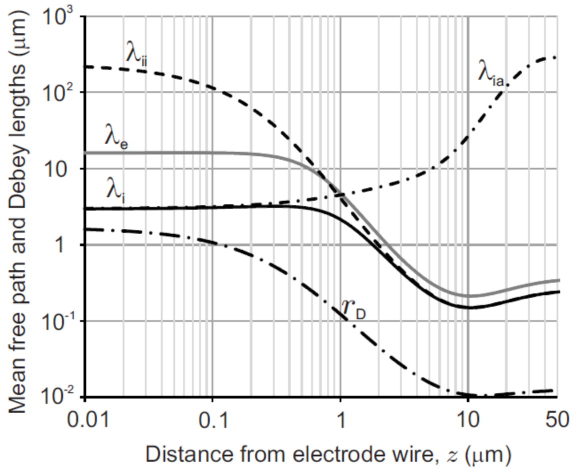

Fig. 3: Space distributions of the mean free path for ion-ion collisions λ_{ii}, ion-atom collisions λ_{ia}, ion total λ_i, electron total λ_e and Debye screening length r_D.

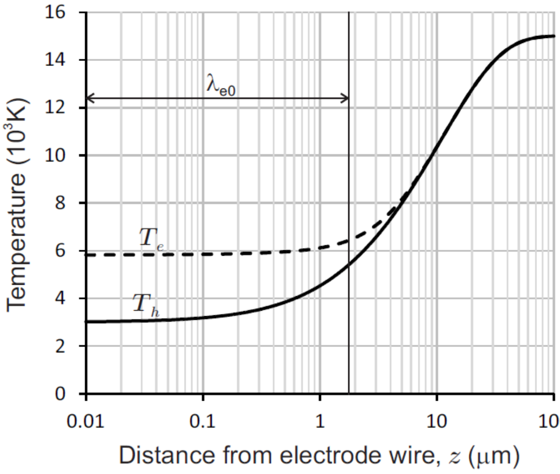

Fig. 4: Temperature space distribution in electrode layer: dashed curve is the electron temperature; solid curve is the temperature of heavy component.

$$f_{1,2} = n_2 Q_{1,2} \sqrt{v_{T_1}^2 + v_{T_2}^2} \tag{12}$$

where n_2 is the target particle number density; $Q_{1,2}$ is the particle collision cross section.

The collision cross section of the neutral particles is determined by their radiuses, for example, the atom-atom collision is described by cross section $Q_{aa} = \pi(r_a + r_a)^2 = 4\pi r_a^2$. The collision cross section of the charged particles is determined by impact parameter $b_0 = e^2/3k_B T_e$ (for single charge) [24], for example, the electron-ion collision is described by cross section $Q_{ei} = \pi b_0^2 \ln\Lambda$, where $\ln\Lambda = \ln(r_D / b_0)$ is the Coulomb logarithm, $r_D = \sqrt{k_B T_e / 8\pi e^2 n_0}$ is the Debye screening length, where T_e is the electron temperature [3, 4].

Because the temperature varies along z in the boundary layer, the collision frequency also is changed, and those or other kinds of collision can prevail in the different layer areas. Therefore, resulting collision frequency is defined as sum of individual frequencies: $f_e = f_{ei} + f_{ea}$ for electrons and $f_i = f_{ii} + f_{ia}$ for ions (scattering on electrons is neglected because of a little momentum transfer).

Thus, the mean free paths for electrons and ions are

$$\lambda_e = \frac{1}{n_0 Q_{ei} + n_a Q_{ea}}, \qquad \lambda_i = \frac{1}{\sqrt{2}\left(n_0 Q_{ii} + n_a Q_{ia}\right)}. \tag{13}$$

The space distributions of electron and ion mean free paths in the boundary layer are presented in Fig. 3 together with Debye screening length. In addition, the mean free paths for ion-ion and ion-atom collisions are presented in this figure, from which clear that ion-atom collisions dominate at electrode surface. However, the situation becomes reverse outside the Knudsen layer, where $\lambda_{ia} >> \lambda_{ii}$ and, therefore, ion thermalization occurs, i.e. ions acquire common velocity.

The particular interest represents the distance from which electron or ion reaches the electrode surface ($\lambda(z) = z$): for electron this distance is $\lambda_{e0} \cong 1.7\mu m$ and for ion $\lambda_{i0} \cong 1.4\mu m$ in the system under consideration.

It should be taken into account that electron mean free path is greater than ion and atom ones. Therefore, cooling of electrons in the boundary layer must lag from the temperature of heavy components. The electron temperature can be calculated via consideration of energy transfer in collisions [25]:

$$\frac{dT_e}{d\xi} = \frac{T_h - T_e}{\lambda_e}, \tag{14}$$

where $\xi = z_b - z$ is the coordinate which is digitized from the sheath boundary z_b, where $\xi = 0$ and $T_e = T_h$; $\lambda_e = \lambda_e(\xi)$ and $T_h(\xi)$ is described by Eq. (5).

The result of numerical solving of Eq. (14) for $z_b = 50$ μm is presented in Fig. 4. This solution is approximated well by following function:

$$T_e(z) = T_h(z) + \left(T_{pl} - T_w\right)\exp\left(-\frac{z}{\lambda_{e0}} + 0.92\ln\frac{T_w}{T_{pl}}\right), \tag{15}$$

from which follows that electron temperature at the anode surface is $T_{ew} \sim 5800$ K. For molten pool equations (4) and (14) should be solved with temperature $T_m = 2000$ K. Then electron temperature at the cathode surface is $T_{em} \sim 5000$ K.

The Coulomb logarithm, which is necessary for calculation of electron and ion mean free pathes, contains the Debye screening length, which depends on the electron temperature. Meantime, the parameter λ_{e0} is necessary for calculation the electron temperature by equation (15). This problem was solved by approximation method, where λ_{e0} was chosen as a parameter for minimization of difference between input and output values. Thus, the dependencies (5) and (15) were taking into account for calculation of particle mean free paths $\lambda(z)$ and Debye screening length $r_D(z)$, which are presented in Fig. 3.

2.4. Equilibrium electric potential. The welding arc is the nonequilibrium system with high value of current. However, it can be considered as a hypothetical equilibrium system without current, where current causes the deviation from equilibrium values.

The electric potential space distribution between two flat electrodes in the equilibrium plasma as solution of Poisson equation is presented in Jacobi elliptic functions [26]. If the distance between electrodes $L > 8r_D$, the potential space distribution with respect to the bulk plasma potential can be described in the following form:

$$\Phi(x) = \ln\left[\left(\tanh\frac{x - x_w^{\inf}}{2}\right)^{-\frac{2\Phi_w^s}{|\Phi_w^s|}}\left(\tanh\frac{x_m^{\inf} - x}{2}\right)^{-\frac{2\Phi_m^s}{|\Phi_m^s|}}\right], \tag{16}$$

where $\Phi = e\phi/k_BT$ is the dimensionless relative potential; $x = z/r_D$ is the dimensionless coordinate; Φ_w^s is the dimensionless relative potential of welding wire with coordinate $z = 0$; Φ_m^s is the dimensionless relative potential of molten pool with coordinate z

$= L$; $x^{\inf}$ is a value of the coordinate which approaching the potential asymptotically tends to infinity: $x_w^{\inf} = \ln\left|\tanh\left(\Phi_w^s/4\right)\right|$, $x_m^{\inf} = L/r_D - \ln\left|\tanh\left(\Phi_m^s/4\right)\right|$.

Boundary relative potential distributions can be obtained from Eq. (16) in a semi-infinite approach for wire electrode

$$\tanh\left(\frac{\Phi_w(z)}{4}\right) = \tanh\frac{\Phi_w^s}{4}\exp\left(-\frac{z}{r_D(z)}\right), \tag{17}$$

and for molten pool

$$\tanh\left(\frac{\Phi_m(z)}{4}\right) = \tanh\frac{\Phi_m^s}{4}\exp\left(\frac{z-L}{r_D(z)}\right). \tag{18}$$

The resulting total potential is the sum $\varphi = \phi + \varphi_{pl}$, where the bulk plasma potential φpl characterizes the size of operation that is necessary for the plasma to gain some volumetric charge [27]. The bulk plasma potential φ_{pl} for the plasma layer is determined by both boundary conditions [26],

$$\varphi_{pl} = -2\frac{k_B T_{pl}}{e}\tanh\left(\frac{\Phi_w^s + \Phi_m^s}{4}\right). \tag{19}$$

The equilibrium relative potential of electrode (without current) is determined via balance of the electron and ion fluxes on the electrode surface, and in the collisionless plasma it is represented as the floating potential of Langmuir probe with taken into account the thermionic emission from electrode, which is described by Richardson's equation

$$j_{eT}^w = \frac{4\pi m_e\left(k_B T_w\right)^2}{\left(2\pi\hbar\right)^3}\exp\left(-\frac{W_{eff}}{k_B T_w}\right), \tag{20}$$

where $W_{eff} = W - e\sqrt{eE_w}$ is the electrode work function W with Schottky correction; E_w is the surface field strength [26]:

$$E_w = 2\frac{k_B T_{ew}}{e r_D}\sinh\frac{V_w}{2k_B T_{ew}};$$

$V_w = k_B T_{ew}\Phi_w^s$ is the potential barrier in the plasma near electrode wire in the arc current absence. The Schottky correction describes the decrease in electron work function W as a result of the image force action [28] and only for negative potential barrier is applicable.

The electron adsorption flux through the Knudsen layer [29]

$$j_e^w = \frac{1}{4}n_0^w v_{eT}^w \exp\frac{V_w}{k_B T_e^w}, \tag{21}$$

and the ion flux to electrode through the potential barrier

$$j_i^w = \frac{n_0^w}{4}\times\begin{cases} v_{iT}^w \exp\left(-\dfrac{V_w}{k_B T_h^w}\right), & V_w > 0 \\ v_B^w, & V_w < 0 \end{cases}, \tag{22}$$

where $v_{eT}^w = \sqrt{8k_B T_e^w / \pi m_e}$ is the electron thermal velocity; $v_{iT}^w = \sqrt{8k_B T_h^w / \pi m_i}$ is the ion thermal velocity; $v_B^w = \sqrt{k_B\left(T_h^w + T_e^w\right)/m_i}$ is the Bohm velocity [30] and $n_{w0} = n_0(\lambda_{i0})$ is the unperturbed number density outside the collisionless Knudsen layer [2], at the distance λ_{i0} from electrode (see Fig.4);$T_e^w = T_e\left(\lambda_{e0}\right) \sim 6400\text{K}$ and $T_h^w = T_h\left(\lambda_{i0}\right) \sim 5000\text{K}$K. The ion flux from electrode, which is caused by evaporation $(j_{0Fe}/m_i)\, exp[(W - E_{ion})/k_B T_w]$, can be neglected because it much less than others.

Hence, the equilibrium potential barrier in the plasma near electrode without current

$$\Phi_w^s = \ln\left[\frac{v_B^w}{v_{eT}^w} + \frac{v_e(T_w)}{n_0^w}\sqrt{\frac{T_w}{T_e^w}}\exp\left(-\frac{W_{eff}}{k_B T_w}\right)\right]. \tag{23}$$

The equilibrium potential barrier near molten pool is determined by following equation

$$\Phi_m^s = \ln\left[\frac{v_B^m}{v_{eT}^m} + \frac{v_e(T_m)}{n_0^m}\sqrt{\frac{T_m}{T_e^m}}\exp\left(-\frac{W_{eff}}{k_B T_m}\right)\right], \tag{24}$$

where v_{eT}^m is the electron thermal velocity; v_{iT}^m is the ion thermal velocity; v_B^m is the Bohm velocity and n_0^m is the unperturbed number density at the molten pool.

In the system under consideration the equilibrium relative potentials are: $\Phi_w^s = -4.6$ ($\varphi_w^s = -2.3$V) and $\Phi_m^s = -5.7$ ($\varphi_m^s = -2.5$V). The bulk plasma potential is $\varphi_{pl} = 2.6$V.

The total potential space distribution $\varphi(z) = \phi(z) + \varphi_{pl}$ is presented in Fig. 5 together with field distribution, which strength is determined by following equation [26]

$$E(z) = 2\frac{k_B T_e(z)}{e r_D(z)}\sinh\frac{e\varphi(z)}{2k_B T_e(z)}. \tag{25}$$

Presented in figure 5 potential and field distributions are calculated for the plasma without arc current and correspond to modeling of authors [1] for low current and electrode temperatures of 3000 K and 4000 K. The electrode potential barrier decreases with increasing T_w.

2.5. Electric current across arc. The total arc voltage U_c can be presented as sum of voltage drops at electrode wire δU_w, at arc column δU_{arc} and at molten pool δU_m:

$$U_c = \delta U_w + \delta U_{arc} + \delta U_m.$$

In addition, the current I_c through system allows defining all voltage drops. In present consideration, when electrode wire is anode, U_c and I_c are positive, when current directed from electrode wire to molten pool.

Ohm's Law determines the current across arc column

$$I_c = A_{arc}\sigma_{arc}E_{arc}, \tag{26}$$

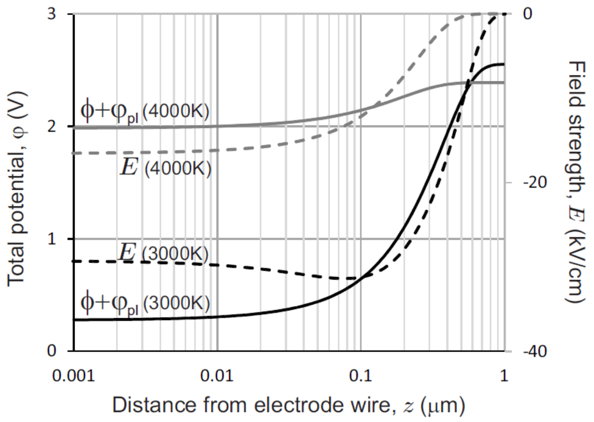

Fig 5: Space distribution of the total potential φ (solid) and field E (dashed) in equilibrium boundary layer for electrode temperature 3000 K (black) and 4000 K (grey).

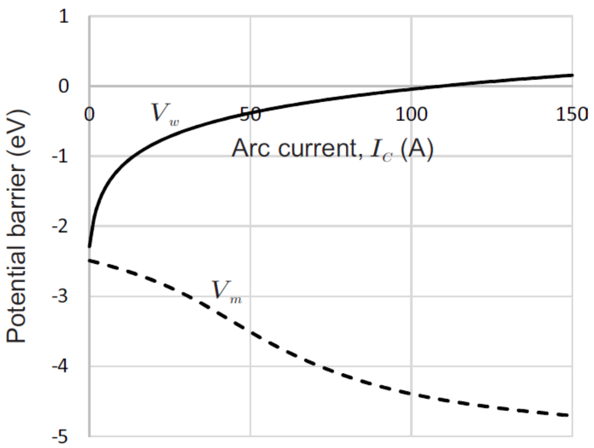

Fig 6: Dependencies of potential barrier height on the arc current for electrode wire (solid) and molten pool (dashed)..

where $A_{arc} = \pi d_{arc}^2 / 4$, d_{arc} is the average arc diameter; σ_{arc} is the average electrical conductivity in LTE arc region,

$$\sigma_{arc} = \frac{e^2}{m_e\left(Q_{ei} + Q_{ea}\right)v_{Te}} + \frac{e^2}{m_i\left(Q_{ii} + Q_{ia}\right)v_{Ti}}, \tag{27}$$

$v_{Te(i)} = \sqrt{8k_B T_{pl} / \pi m_{e(i)}}$ is the thermal velocity in arc region; E_{arc} is the field, which is defined by the arc voltage drop and arc length: $E_{arc} = \delta U_{arc}/L$.

Hence, the voltage drop at arc column as a function of current is

$$\delta U_{arc} = \frac{I_c L}{A_{arc}\sigma_{arc}}. \tag{28}$$

The potential barrier in the plasma near electrode wire is determined by equilibrium value and voltage drop:

$$V_w = e\varphi_w^s + e\delta U_w, \tag{29}$$

where φ_w^s is the equilibrium relative potential (without current) of electrode wire, which is defined by Eq. (23): $\varphi_w^s = k_B T_e^w \Phi_w^e / e$.

The current through electrode wire surface is the sum of emission current and currents of electron and ion fluxes to electrode from the plasma through Knudsen layer:

$$I_c = eA_w\left(j_e^w - j_{eT}^w - j_i^w\right), \tag{30}$$

where $A_w = \pi d_w^2 / 4$, d_w is the diameter of anode spot.

Thus, Eq. (30) allows determining the voltage drop on electrode wire as a function of arc current $\delta U_w(I_c)$ via numerical calculation, as a root of equation

$$j_e^w\left(\delta U_w\right) - j_{eT}^w\left(\delta U_w\right) - j_i^w\left(\delta U_w\right) - I_c / eA_w = 0.$$

The current through molten pool is the sum:

$$I_c = eA_w\left(j_{eT}^m + j_{eE}^m + j_i^m - j_e^m\right), \tag{31}$$

where $A_m = \pi d_m^2 / 4$, where d_m is the diameter of cathode spot on the molten pool and current components are defined by similar equations, but with others parameters and signs. Besides, it should be considered that high potential barrier near cathode provides the field emission with flux j_{eE}^{m}. The inward current in molten pool is positive and potential barrier remains negative:

$$V_m = e\varphi_m^s - e\delta U_m, \tag{32}$$

where φ_m^s is the equilibrium relative potential of molten pool, which is defined by Eq. (24).

The thermionic emission flux is

$$j_{eT}^{m} = \frac{4\pi m_e \left(k_B T_m\right)^2}{\left(2\pi\hbar\right)^3}\exp\left(-\frac{W_{eff}}{k_B T_m}\right).$$

The field emission is described by Fowler-Nordheim equation:

$$j_{eE}^{m} = \frac{e^3 E_m^2}{16\pi^2 \hbar W_{eff}}\exp\left(-\frac{4\sqrt{2m_e}\,W_{eff}^{3/2}}{3e\hbar E_m}\right).$$

The electron flux through Knudsen layer and the ion flux are

$$j_e^{m} = \frac{1}{4} n_0^m v_{eT}^m \exp\left(\frac{V_m}{k_B T_e^m}\right), \qquad j_i^m = \frac{1}{4} n_0^m v_B^m .$$

Then, Eq. (31) allows determining the voltage drop on molten pool as a function of arc current $\delta U_m(I_c)$. The dependencies of potential barrier heights (29) and (32) on the arc current are presented in Fig. 6 for electrode wire (V_w) and molten pool (V_m). The following parameters were used: diameter of wire anode spot d_w = 1.2mm (on the tip of electrode wire the metal droplet is formed in the welding process, and diameter of this droplet can exceed wire diameter); arc column average diameter d_{arc} = 5 mm; diameter of molten pool cathode spot d_m = 6 mm; arc length L = 14 mm; T_w = 3000K; T_m = 2000K; T_{pl} = 15000 K.

The total arc voltage is

$$U_c\left(I_c\right) = \frac{I_c L}{A_{arc}\sigma_{arc}} + \delta U_w\left(I_c\right) + \delta U_m\left(I_c\right), \tag{33}$$

and potential distribution between electrode wire and grounded molten pool can be describe by following equations

$$\begin{cases} \varphi(I, z) = \phi_w(I, z) + \phi_m(I, z) + \varphi_{pl}(I, z) \\ \phi_w(I, z) = \dfrac{4k_B T_{ew}}{e}\operatorname{atanh}\left[\tanh\dfrac{e\varphi_w^s + e\delta U_w(I)}{4k_B T_{ew}}\exp\left(-\dfrac{z}{r_D(z)}\right)\right] \\ \phi_m(I, z) = \dfrac{4k_B T_{em}}{e}\operatorname{atanh}\left[\tanh\dfrac{e\varphi_m^s - e\delta U_m(I)}{4k_B T_{em}}\exp\left(\dfrac{z-L}{r_D(L-z)}\right)\right] \\ \varphi_{pl}(I, z) = \dfrac{I_c(L-z)}{S_{arc}\sigma_{arc}} - \phi_m(I, L) \end{cases}. \tag{34}$$

From calculations follows that basic voltage drop happens in the thin plasma layer near cathode (molten pool), which is caused by need to maintain the large field strength for effective electron emission. The potential barrier near anode surface remains negative at small currents. The increase in current leads to change of the barrier sign to positive.

3. ***Heat transfer in arc and metal vapor generation.*** The electron and ion currents provide not only transport of charges, but also energy transfer through electrode surface. It should be considered that collision of ion with electrode wire (anode) leads to its neutralization and provides transfer of the potential energy, which is equal to ($E_{ion}-W$), and the kinetic energy, which is defined by the average ion motion energy outside the Knudsen layer $3k_BT_h^w/2$ and by the energy of acceleration in the sheath electric field $-V_w$ [3], if the potential barrier $V_w < 0$. Thus, flow of energy transfer via ion-anode collisions is described by equation

$$\Gamma_i^w = A_w j_i^w \times \begin{cases} \left(E_{ion} - W - V_n + \frac{3}{2}k_B T_h^w\right), & V_w < 0 \\ \left(E_{ion} - W + \frac{3}{2}k_B T_h^w\right), & V_w \geq 0 \end{cases}.$$

In this case, the work function without Schottky correction is used, because the image-force concept, which is a source of Schottky effect, is inapplicable to the electron exchange between adsorbed ion and electrode surface.

The adsorbed electron provides transfer of energy, which is equal to sum of the average motion energy $3k_BT_e^w/2$, the energy of acceleration V_w, if the potential barrier is positive, and the work function as a potential energy. The flow of energy transfer via electron adsorption is described by equation

$$\Gamma_i^w = A_w j_i^w \times \begin{cases} \left(E_{ion} - W - V_n + \frac{3}{2}k_B T_h^w\right), & V_w < 0 \\ \left(E_{ion} - W + \frac{3}{2}k_B T_h^w\right), & V_w \geq 0 \end{cases}$$

The electron leaving the anode via emission provides loss in energy, which is equal to the work function:

$$\Gamma_{em}^w = A_w j_{em}^w \times \begin{cases} W_{eff}, & V_w < 0 \\ W, & V_w \geq 0 \end{cases}.$$

The evaporation flux (6) provides loss in energy:

$$\Gamma_{vap}^w = A_w j_{0Fe} c_p T_w.$$

Thus, the total heat flow to electrode wire is described by following equation

$$\Gamma_w = \Gamma_i^w + \Gamma_e^w - \Gamma_{em}^w - \Gamma_{vap}^w - A_w \varepsilon_w \sigma_{SB} T_w^4 - A_w k_k \nabla T_w, \tag{35}$$

where $\varepsilon_w \sigma_{SB} T_w^4$ is the heat flux, which occurs via radiation, ε_w is the emissivity of the welding wire, σ_{SB} is the Stefan-Boltzmann constant; $\kappa_w \nabla T_w$ is the heat flux along the electrode wire with thermal conductivity κ_w.

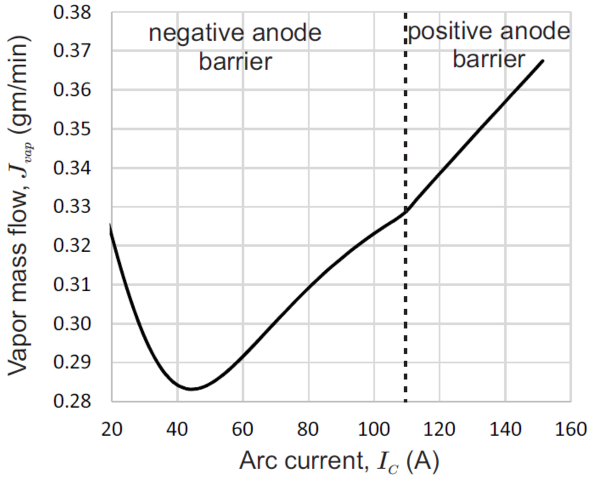

Fig. 7: Vapor formation rate.

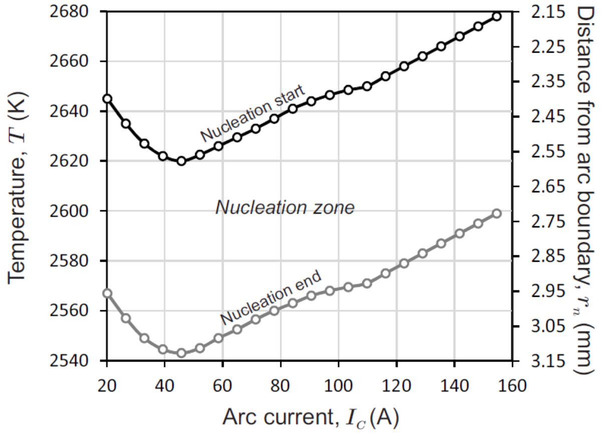

Fig. 8: Dependencies of the temperature of nucleation start and finish; and the distances from arc boundary to beginning and end of nucleation zone on the arc current

This heat flow should be counterbalanced with backflow heat transfer from electrode wire to molten pool by the metal droplets:

$$\Gamma_{drop} = \Gamma_w.$$

The molten metal in the form of droplets or spray transfers to molten pool and provides the energy inflow. The total heat flow in molten pool is described by the following equation (with neglected of Γ_{drop} change during transfer through arc column):

$$\Gamma_m = \Gamma_{drop} + \Gamma_i^w + \Gamma_e^w - \Gamma_{em}^w - A_m \sigma_{SB} T_m^4 - A_m k_m \nabla T_m, \qquad (36)$$

where

$$\Gamma_i^m = A_m j_i^m \left(E_{ion} - W - V_m + \frac{3}{2} k_B T_h^m \right),$$

$$\Gamma_e^m = A_m j_e^m \left(W_{eff} + \frac{3}{2} k_B T_h^m \right), \quad \Gamma_{em}^m = A_m \left(j_{eT}^m + j_{eE}^m \right) W_{eff}.$$

Under stationary conditions, the inflow of heat in molten pool Γ_m should be counterbalanced with outflow of heat via metal evaporation and spraying to environment. Therefore, if spraying of metal from molten pool is neglected, flow of metal vapor

$$\Gamma_{vap} = \Gamma_m.$$

Fig. 7 demonstrates the dependency of vapor mass flow, which emitted by molten pool,

$$J_{vap} = \frac{\Gamma_{vap}}{c_p T_m} \qquad (37)$$

on the arc current, which corresponds with experimental data [31, 32]. Growth of current leads to increase in the potential barrier $-V_m$, that causes increase in heat flow Γ_i^m and reducing of Γ_e^m. These competing trends cause existence of the minimum in dependence, which is presented in Fig. 7.

The potential barrier near electrode wire *Vw* change its sign at some value of arc current. This change provides sharp increase in energy flow, which is transferred from the plasma to anode by conductivity electrons, because they are accelerated in positive potential barrier. This effect can be a reason for transition of metal transfer in welding process from globular to spraying regime [33].

4. Metal vapor condensation and formation of primary particles.

4.1. Vapor ionization. The high-temperature metal vapor from welding arc mixes with shielding gas under the welding torch nozzle. The numerical simulation [34] demonstrates that the gas average temperature in the boundary region at the torch outlet $T \sim 2500$ K. It means that condensation of metal vapor occurs in the vaporshielding gas mixture, before mixing with air.

The high-temperature vapor contains several elements, which concentrations depend on compositions of electrode and welding material. However, for simplicity, it is possible to assume that vapor contains only iron atoms. The flow of iron vapor (37) is mixed with shielding gas, and the mixture flow divergence can be described by equation, similar to Eq. (7). Thus, it is possible to determine the available for ionization atom number density as a function of distance from arc boundary *r* in the following form

$$n_A(r) = \frac{J_{vap}}{m_a A_m v_{vap}} \exp\left(-\frac{r}{l_{mix}}\right), \tag{38}$$

where m_a is the iron atom mass; $v_{vap} \sim 10$m/s is the vapor flow velocity; l_{mix} isthe mixing length scale, which is determined experimentally and in the system under consideration $l_{mix} \sim 1.7$ cm [35, 36].

The mixing of high-temperature vapor with cold shielding gas also determines the temperature of mixture, which can be described by following equation [36]

$$T(r) = T_{sg} + \left(T_{vap} - T_{sg}\right)\exp\left(-\frac{r}{l_{mix}}\right), \tag{39}$$

where $T_{sg} = 300$K is the temperature of shielding gas; $T_{vap} = 3000$K is the temperature of vapor.

Ionization of atoms Eq. (38) can occur by electron impact or by UV radiation. In the paper [20] was demonstrated that relaxation time of UV ionization at the arc boundary $\tau_{UV} \sim 10$ μs, and for thermal impact ionization such relaxation time $\tau_T \sim 0.02$ μs, that is much less. Therefore, it is possible to describe atoms' ionization by Saha equation (10) and determine the unperturbed number density as

$$n_0(r) = \frac{K_S(r)}{2}\left(\sqrt{1 + 4\frac{n_A(r)}{K_S(r)}} - 1\right), \tag{40}$$

with taken into account Eqs. (38) and (39).

4.2. Nucleation. The cooling of vapor-gas mixture provides the increase in supersaturation $S = p/p_{sat}$, where $p = n_A/k_B T$ is the partial pressure of iron vapor, and at some distance from arc boundary *rn* condensation begins, when $S \geq 1$. The condensation occurs in the plasma as a heterogeneous ion-induced nucleation and provides the change in Gibbs free energy ΔG, which is described in the papers [37, 38, 39], where was taken into account the exchange of charges and energy between nucleus and environment:

$$\Delta G = 4\pi a^2\gamma - \frac{4}{3}\pi a^3 \frac{\rho k_B T}{m_a}\ln S + E_\gamma + E_{ex} + E_q;$$

$$E_\gamma = -\frac{Z_n V_b}{2}; \quad E_{ex} = -Z_n\left(W_n - E_{ion}\right); \quad E_q = \frac{e^2}{2}\left(\frac{Z_n^2+1}{a} - \frac{1}{r_1}\right);$$

where a is the nucleus radius; $\gamma = \gamma_0 a/(a + 2\delta)$ is the surface free energy of the nucleus; γ_0 is the surface free energy of the flat; δ is the Tolmen length; m_a is the mass of the condensable atoms; ρ is the nucleus density; S is the supersaturation of the condensable material; Z_n is the nucleus charge number; ε is the dielectric constant; r_i is the radius of the single-charged positive ion, which induced the nucleation; E_γ is the change in surface free energy as a result of the electrical double layer on the nucleus surface; E_{ex} is the change in Gibbs free energy as a result of the interphase energy exchange; E_q is the change in Gibbs free energy as a result of the nucleus charging.

The temperature of nucleation start together with distance between nucleation zone and arc boundary r_n in Fig. 8 is demonstrated as a function of arc current I_c. This dependence is similar to dependence in Fig. 7, because vapor flow from arc J_{vap} determines the iron partial pressure in vapor-gas mixture and, accordingly, the supersaturation.

It should be noted, that the plasma not contains atoms of alkali metals when GMAW is used. Therefore, the iron atoms execute both functions: a source of ionization and a source of nucleation, i.e. the plasma ionization balance is provided by ions of iron, which number density n_i should be excluded from atom number density, which available for nucleation. This feature was described in paper [36], from which the equation for number density of nuclei follows:

$$n_n = \frac{n_A - n_0}{N_{an} + N_{an}^{-3/2}\exp\dfrac{\Delta G(a_n)}{k_B T}}, \tag{41}$$

where $N_{an} = 4\pi\rho a_n^3 / 3m_a$ is the number of atoms in the nucleus; ρ is the nucleus density; $\Delta G(a_n)$ is the change in Gibbs free energy under formation of equilibrium nucleus with radius an.

In the welding fume from GMAW equilibrium nucleus number density much greater equilibrium (Saha) electron and ion number densities [36]. Because ions are the centers of ion-induced nucleation, they disappear from gas phase under nucleation and electron-ion recombination is replaced by the neutralization of nuclei, which have initial positive charge. As a result, the balance between ionization and recombination is broken in favor of ionization, and new electrons and ions appear in the plasma via impact atom ionization, until electrons are being captured by nuclei. Therefore, achievement of equilibrium nucleus number is the time-phased process, which includes additional atom ionization and formation of additional nuclei until equilibrium will be reached.

The appearance of nuclei creates a new ionization-recombination channel. Atom ionization and ion recombination occurs via interaction with nucleus surface. Surface atom ionization degree is described by well-known Saha-Langmuir equation [40]. When the first nuclei are formed, their large number causes the capturing of electrons and leads to change of ionization mechanism. Initial thermal ionization is replaced by ionization via nuclei surface. Accordingly, the energy exchange term in Gibbs free energy is also replaced: the electron transition between nucleus Fermi level and valence electron level of the adsorbed atom should be used instead of transition between nucleus and gas. Surface atom ionization and ion recombination provide increase in ion number density. Thus, welding fume plasma in nucleation zone consist mainly of positive ions and nuclei with average negative charge if GMAW is used [41].

The two kinds of nuclei are formed by the heterogeneous ion-induced nucleation: the equilibrium nuclei with radius a_n, which are in the equilibrium state with the environment; and the nonequilibrium critical nuclei with radius a_{cr}, which appear as a result of fluctuations. The radius of the equilibrium nucleus is determined as a minimum of the function $\Delta G(a)$, and the radius of the critical nucleus is determined as the maximum of the function $\Delta G(a)$. The equilibrium nucleus is in the stable stage and some activation energy is necessary for the nucleus growth $E_{act} = \Delta G(a_{cr}) - \Delta G(a_n)$. This activation energy decreases down to zero ($E_{act} \to 0$) with the vapor-gas mixture cooling. After that, the unrestricted growth of nuclei begins, until the condensable materials do not deplete. The temperature, which corresponds to nucleation termination in Fig. 8 also is presented as a function of arc current.

4.3. Droplet growth. The nuclei growth occurs via two mechanisms: condensation growth and coagulation, which is a coalescence, because nuclei are in the liquid state. Condensation growth of nucleus with radius *an* is determined by the increment in the mass due the adsorption and transpiration fluxes difference, and is described in the free molecular regime by following equation [35]

$$\frac{da_n}{dt} = \frac{\alpha_c v_{Ta} m_a n_a}{4\rho}\left(1 - \frac{S_R}{S}\right), \tag{42}$$

where α_c is the eveporation-condensation coefficient [42]; $n_a = n_A - n_i - N_{an} n_n$ is the number density of iron atoms in the gas phase; S is the current supersaturation; $S_R = p_{sat}(a_n)/p_{sat}(\infty)$ is the change in vapor partial pressure at the account of the surface curvature and interphase interaction.

The large number density of nuclei $n_n \sim 10^{16}$ cm^{-3} causes their intensive Brownian collisions and coalescence. As a result, the coagulated droplets with radius a_{cd}, which grow through coalescence and condensation are formed. However, it is necessary to take into account that the nucleation continues, and the system thermodynamics requires the presence of the nuclei with equilibrium number density (41). Therefore, number and size of nuclei in the nucleation zone cannot change via coalescence, because new nuclei appear. This requirement is removed after the nucleation termination.

Thus, already at the initial stage of nucleation the bimodal size distribution of the droplets occurs. The first mode contains the droplets of nuclei; coagulated droplets resulting from the long-term coalescence and condensation represent the second mode. It should be noted that in this case nucleation is the original “pump” for the transfer of the atoms from the gas phase into the coagulated droplets, and intensity of this process can be higher than the intensity of the vapor condensation (42) on the aggregated droplets [43].

Droplets can be described by a log-normal size distribution, which is based on the number of atoms *N* contained in the droplets, using probability density function for two modes:

$$f_n(N)=\frac{n_n}{N\sqrt{2\pi}\ln\sigma_n}\exp\frac{-\left(\ln N-\ln N_{an}^m\right)^2}{2\ln^2\sigma_n},$$

$$f_{cd}(N)=\frac{n_{cd}}{N\sqrt{2\pi}\ln\sigma_{cd}}\exp\frac{-\left(\ln N-\ln N_{cd}^m\right)^2}{2\ln^2\sigma_{cd}}$$

$$f_N=f_n(N)+f_{cd}(N)\,, \tag{43}$$

where index *n* is used for nuclei, index *cd* is used for coagulated droplets; $N^m=\overline{N}_a exp(-ln^2\sigma/2)$ is the median of distribution; *σ* is the standard deviation; $\overline{N}_a$ is the average number of atoms in the droplets.

The evolution of such a system can be described by the integral moments of the distribution (43) [43]. The moments are described by the following equation:

$$M(k)=\int_0^\infty N^k f_N dN\,,$$

and the Brownian coagulation can be described as

$$\frac{\partial M(k)}{\partial t}=\frac{1}{2}\int_0^\infty f_N\int_0^\infty \beta(N,N')f_N'\left[(N+N')^k-N^k-N'^k\right]dN'dN\,, \tag{44}$$

where *N* and *N'* are the numbers of atoms in the colliding droplets; β(*N,N'*) is the collision kernel. The Brownian collision kernel can be determined by the kinetic theory of gases, or by the diffusion theory according to droplet size. If the droplets are much smaller than mean free path of the gas particles, the gas-kinetic theory should be used to determine the collision kernel

$$\beta(N,N')=\beta_0\left(N^{1/3}+N'^{1/3}\right)^2\sqrt{\frac{N+N'}{NN'}},\quad \beta_0=\left(\frac{3m_a}{4\pi\rho}\right)^{1/6}\sqrt{\frac{6k_BT}{\rho}}\,,$$

where Coulomb interaction is neglected.

The evolution of the moments (44) can be determined for each mode (43). The zero moments represent the total number densities of the generated particles n_n and n_{cd}. The total numbers of atoms in these are determined by the first moments. As a result, the average number of atoms in the droplets of each mode is

$$\overline{N}_n=\frac{M_n(1)}{M_n(0)};\qquad \overline{N}_{cd}=\frac{M_{cd}(1)}{M_{cd}(0)}\;; \tag{45}$$

and the standard deviations are defined by the following equations:

$$\ln^2 \sigma_n = \ln \frac{M_n(0) M_n(2)}{M_n(1)^2}, \quad \ln^2 \sigma_{cd} = \ln \frac{M_{cd}(0) M_{cd}(2)}{M_{cd}(1)^2}. \tag{46}$$

Equations (43)-(46) allow to describe the evolution of the coalescence in the bimodal system of droplets with taking into account both the intramodal coalescence and the intermodal association of the different droplet modes.

The growth of droplets occurs in the cooling environment and continues up to phase transition. The temperature of the phase transition depend on the droplet radius [44], i.e. the droplets of the coagulated mode (the melting point is about 1730 K) solidify earlier, than droplets of the nuclei mode (the melting point is about 1330 K); and exists the transient stage, when the coagulated mode is presented by solid particles, but the nuclei mode is the liquid droplets. The bimodal coalescence terminates, when coagulated droplets become the solid particles. There is only coalescence of the nuclei mode.

Calculation of the droplets' growth gives the parameters of primary particles size distribution after solidification, which is presented in the table 1. Increase in the arc current leads to growth of particles' sizes, but their number densities are changed little, because vapor flow rate is increased with current.

5. Formation of welding fume via coagulation of primary particles.

The agglomerates generated from the solid primary particles are the irregular structures; therefore, the radius of agglomerate, which contains N primary particles (monomers), is described as $r_{ag} = aN^{1/D_f}$, where a is the radius of the monomers; D_f is the fractal dimension ($D_f = 3$ for perfect sphere).

The collision kernel for the free molecule regime without electrical interaction between particles is described by the following equation [45]:

$$\beta(N, N') = \beta_0 \left(N^{1/D_f} + N'^{1/D_f} \right)^2 \sqrt{\frac{N + N'}{NN'}}, \quad \beta_0 = \sqrt{\frac{6k_B T_a}{\rho}}, \tag{47}$$

where ρ is the monomer density; N and N' are the numbers of monomers in the colliding agglomerates with fractal dimension D_f.

The collision kernel for charged particles is [46]

$$\beta_Q(N, N') = \beta(N, N') \exp \frac{-U_{N,N'}}{k_B T},$$

where $U_{N,N'}$ is the interaction energy on the shortest distance between the interacting particles, which can be considered in the Coulomb approximation

$$U_{N,N'} = \frac{e^2 Z_N Z_{N'}}{a\left(N^{1/D_f} + N'^{1/D_f} \right)},$$

where Z_N and Z'_N are the particle charges divided by the elementary charge, which are determined by following equation [47]

$$Z_N = \frac{k_B T r_D}{2e^2} \sinh \frac{2aN^{1/D_f} V_b}{r_D k_B T}, \tag{48}$$

which under condition $r_{ag} V_b \ll r_D k_B T$ can be described in Coulomb approach:

Table 1: Characteristics of the primary particles

	Minimum sizes	Maximum sizes
$\bar{d}_n$ (nm)	4.1	4.7
n_n (cm^{-3})	3.1×10^{14}	2.6×10^{14}
$\bar{d}_{cd}$ (nm)	8.3	9.5
n_{cd} (cm^{-3})	4.2×10^{13}	3.5×10^{13}
I_c (A)	45	115

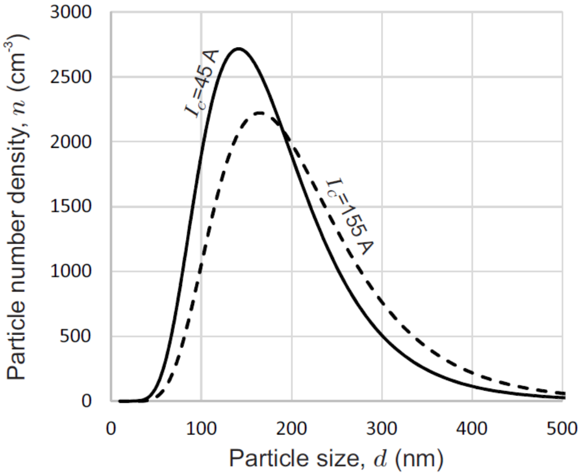

Fig 9: Inhalable particle size distributions for arc current I_c = 45A (solid) and I_c = 155A (dashed)

$Z_N \cong aN^{1/D_f} V_b / e^2$.

The resulting collision kernel is

$$\beta_Q(N,N') = \beta(N,N') \exp \frac{-a_{N,N'} V_{bN} V_{bN'}}{e^2 k_B T}\ , \tag{49}$$

where $a_{N,N'} = a(NN')^{1/D_f}(N^{1/D_f} + N'^{1/D_f}) - 1$.

The calculation of coagulation is carried out in the free molecular regime by method of moments while agglomerates' sizes less than mean free path of the gas particles. When sizes exceed the mean free path length, Eq. (49) becomes inapplicable. In this case the collision kernel should be described in the diffusion regime:

$$\beta_Q(N,N') = \frac{2k_B T C(a_{N,N'})}{3\eta} \frac{a\left(N^{1/D_f} + N'^{1/D_f}\right)}{a_{N,N'}} \left(1 + \frac{a_{N,N'} V_{bN} V_{bN'}}{e^2 k_B T}\right), \tag{50}$$

where η is the viscosity; $C(a)$ is the Canningham slip correction [48]

$$C(a) = 1 + \frac{\lambda}{a}\left(1.142 + 0.588 \exp\left(-\frac{a}{\lambda}\right)\right),$$

λ = 67nm is the mean free path.

The calculation results presented in Fig. 9 as the inhalable particle size distributions for two values of the arc current, which correspond to minimum and maximum high-temperature vapor flow rates.

6. Conclusion.

Thus, modeling of processes, which are occur in the electric arc during arc welding, allows determining the rate of high-temperature vapors efflux from molten pool to environment. It is very important parameter, because metal vapors' condensation is a source of welding fumes and inhalable particles in the breathing zone [35, 39, 49].

The equilibrium in contact of electrode wire or molten pool with plasma, which is produced by arc, provides the negative potential barrier in the plasma near electrodes. The electric current across the arc provides increase in negative barrier near cathode and its decreasing near anode (the electrode wire is anode in the system under consideration). At some value of current the change in barrier sign occurs and further current amplification leads to increase in the positive potential barrier near anode. The change in potential barrier sign provides sharp increase in energy flow, which is transferred from the plasma to anode by conductivity electrons, because they are accelerated in positive potential barrier. This effect can be a reason for transition of metal transfer in welding process from globular to spraying regime.

Increase in the arc current leads to growth of high-temperature vapor flow rate from welding arc to environment and provides increase in the size of solid primary particles, because occurs the shift of nucleation zone toward the arc, i.e. in the area with higher temperature; and, accordingly, increase in the time duration of droplets' growth. This tendency persists in the inhalable particle size distribution after coagulation of primary particles, what is correlated with experimental data [50]. Thus, the fumes produced by welding with high current can easier be filtered.

References:

1. *N.A. Almeida, M.S. Benilov, G.V. Naidis* Unified modelling of nearcathode plasma layers in high-pressure arc discharge, Journal of Physics D: Applied Physics 41 (2008) 245201.
2. *M. Baeva, M.S. Benilov, N.A. Almeida, D. Uhrlandt* Novel non-equilibrium modelling of DC electric arc in argon, Journal of Physics D: Applied Physics 49 (2016) 245205.
3. *M.S. Benilov* Understanding and modelling plasma-electrode interaction in high-pressure arc discharge: a review, Journal of Physics D: Applied Physics 41 (2008) 144001.
4. *V. Colombo, E. Ghedini, P. Sanibondi* Two-temperature thermodynamic and transport properties of carbon-oxygen plasmas, Plasma Sources Science and Technology 20 (2011) 035003.
5. *J. Haidar* The dynamic effects of metal vapour in gas metal arc welding, Journal of Physics D: Applied Physics 43 (2010) 165204.
6. *A. Khrabry, I. Kaganovich, V. Nemchinsky, A. Khodak* Investigation of a short argon arc with hot anode. Part I: numerical simulations of nonequilibrium effects in the near-electrode region, Physics of Plasmas (2018) 013521.
7. *I. Semenov, I. Krivtsun, V. Demchenko, A. Semenov, U. Reisgen, O.Mokrov, A. Zabirov* Modelling of binary alloy (Al-Mg) anode evaporation in arc welding, Modelling and Simulation in Materials Science and Engineering 20 (2012) 055009.
8. *M. Tanaka, M. Ushio, C.S. Wu* One-dimensional analysis of the anode boundary layer in free-burning argon arcs, Journal of Physics D: Applied Physics 32 (1999) 605-611.
9. *M. Schnick, U. Fuessel, M. Hertel, M. Haessler, A. Spille-Kohoff, A.B. Murphy* Modelling of gas-metal arc welding taking into account metal vapour, Journal of Physics D: Applied Physics 43 (2010) 434008.
10. *V.I. Vishnyakov, S.A. Kiro, M.V. Oprya, O.I. Shvetz, A.A. Ennan* Nonequilibrium ionization of welding fume plasmas; Effect of potassium additional agent on the particle formation, Journal of Aerosol Science 113 (2017) 178-188.
11. *V.I. Vishnyakov, S.A. Kiro, M.V. Oprya, A.A. Ennan* Effects of shielding gas temperature and flow rate on the welding fume particle size distribution, Journal of Aerosol Science 114 (2017) 55-61.

12. *I.V. Krivtsun* Anode processes in welding arcs, The PatonWelding Journal 11-12 (2018) 91-104.
13. *I. Langmuir* The interaction of electron and positive ion space charges in cathode sheaths, Physical Review 33 (1929) 954-989.
14. *C.J. Knight* Theoretical modeling of rapid surface vaporization with back pressure, AIAA Journal 17 (1979) 519-523.
15. *H.G. Fan, R. Kovacevic* A unified model of transport phenomena in gas metal arc welding including electrode, arc plasma and molten pool, Journal of Physics D: Applied Physics 37 (2004) 2531-2544.
16. *J. Zhang, X. Luo, Z. Feng, F. Guo* Effects of pin and wire electrodes on flow boiling heat transfer enhancement in a vertical minichannel heat sink, International Journal of Heat and Mass Transfer 136 (2019) 740-754.
17. *A.B. Murphy* The effects of metal vapour in arc welding, Journal of Physics D: Applied Physics 43 (2010) 434001.
18. *U. H¨ogst¨orm* Review of some basic characteristics of the atmospheric surface layer, Boundary-Layer Metrology 78 (1996) 215-246.
19. *F. Valensi, S. Pellerin, A. Boutaghane, K. Dzierzega, S. Zelinska, N. Pellerin, F. Briand* Plasma diagnostics in gas metal arc welding by optical emission spectroscopy, Journal of Physics D: Applied Physics 43 (2010) 434002.
20. *V.I. Vishnyakov, S.A. Kiro, A.A. Ennan* Reducing of UV radiation, ozone concentration and fume formation in gas metal arc welding, Aerosol Science and Engineering 4 (2020) 192-199.
21. *C. Kittel* Thermal Physics, Wiley, New York, 1969.
22. *A. Huczko, A. Szymanski* Thermal decomposition of carbon dioxide in an argon plasma jet, Plasma Chemistry and Plasma Processing 4 (1984) 59-72.
23. *M. Mitchner, C.H. Kruger* Partially Ionized Gases, Wiley, New York, 1973.
24. *B.M. Smirnov* Kinetics of electrons in gases and condensed systems, Physics-Uspekhi 45 (2002) 1251-1286.
25. *R.J. Goldston, P.H. Rutherford* Introduction to Plasma Physics, IOP Publishing, Bristol, 1995.
26. *V.I. Vishnyakov, G.S. Dragan* Electrostatic interaction of charged planes in the thermal collision plasma: Detailed investigation and comparison with experiment, Physical Review E 71 (2005) 016411.
27. *V.I. Vishnyakov, G.S. Dragan, V.M. Evtuhov* Nonlinear Poisson-Boltzmann equation in spherical symmetry, Physical Review E 76 (2007) 036402.
28. *A.G. Milnes, D.L. Feucht* Heterojunctions and Metal-Semiconductor Junctions, Academic Press, New York and London, 1972.
29. *V.E. Fortov, A.G. Khrapak, S.A. Khrapak, V.I. Molotkov, O.F. Petrov* Dusty plasmas, Physics-Uspekhi 47 (2004) 447-492.
30. *K.-U. Riemann* The Bohm criterion and sheath formation, Journal of Physics D: Applied Physics 24 (1991) 493-518.
31. *R.F.Heile, D.C. Hill* Particulate fume generation in arc welding processes, Welding Journal 54 (1975) 201s-210s.
32. *I. Pires, L. Quintino, R.M. Miranda, J.F.P. Gomes* Fume emissions during gas metal arc welding, Toxicological and Environmental Chemistry 88 (2006) 385-394.
33. *E.J. Soderstrom, P.F. Mendez* Metal transfer during GMAW with thin electrodes and Ar-CO_2 shielding gas mixture, Welding Journal 87 (2008) 124s-133s.

34. *M. Dreher, U. F¨ussel, M. Schnik* in: Mathematical Modelling of Weld Phenomena, v9, Verlag der Technischen Universit¨at Graz, Graz, 2009, pp. 127-138.
35. *V.I. Vishnyakov, S.A. Kiro, M.V. Oprya, O.D. Chursina, A.A. Ennan* Formation of particles in welding fume plasmas: Numerical modeling and experiment, Ukrainian Journal of Physics 64 (2019) 392-405.
36. *V.I. Vishnyakov, S.V. Kozytskyi, A.A. Ennan* Features of nucleation in welding fumes from gas metal arc welding, Journal of Aerosol Science 137 (2019) 105439.
37. *V.I. Vishnyakov* Homogeneous nucleation in thermal dust-electron plasmas, Phisycal Review E 78 (2008) 056406.
38. *V.I. Vishnyakov, S.A. Kiro, A.A. Ennan* Heterogeneous ion-induced nucleation in thermal dusty plasmas, Journal of Physics D: Applied Physics 44 (2011) 215201.
39. *V.I. Vishnyakov, S.A. Kiro, A.A. Ennan* Formation of primary particles in welding fume, Journal of Aerosol Science 58 (2013) 9-16.
40. *M.J. Dresser* The Saha-Langmuir equation and its application, Journal of Applied Physics 39 (1968) 338-339.
41. *V.I. Vishnyakov* Ionization balance in low-temperature plasmas with nanosized dust, Ukrainian Journal of Physics 66 (2021) 303-309.
42. *M. Okuyama, J.T. Zung* Evaporation-condensation coefficient for small droplets, Journal of Chemistry Physics 46 (1967) 1580-1585.
43. *V.I. Vishnyakov, S.A. Kiro, A.A. Ennan* Bimodal size distribution of primary particles in the plasma of welding fume: Coalescence of nuclei, Journal of Aerosol Science 67 (2014) 13-20.
44. *Q. Shu, Y. Yang, Y.Zhai, D.M. Sun, H.J. Xiang, X.G. Gong* Sizedependent melting behavior of iron nanoparticles by replica exchange molecular dynamics, Nanoscale 4 (2012) 6307-6311.
45. *M.K. Wu, S.K. Friedlander* Enhanced power low agglomerate growth in the free molecular regime, Journal of Aerosol Science 24 (1992) 273-282.
46. *V.I. Vishnyakov, S.A. Kiro, M.V. Oprya, A.A. Ennan* Coagulation of charged particles in self-organizing thermal plasmas of welding fumes, Journal of Aerosol Science 76 (2014) 138-147.
47. *V.I. Vishnyakov, S.A. Kiro, M.V. Oprya, A.A. Ennan* Effect of shielding gas temperature on the welding fume particle formation: Theoretical model, Journal of Aerosol Science 124 (2018) 112-121.
48. *Ch. Hagwood, Yu. Sivathanu, G. Mulholland* The DMA transfer function with Brownian motion a trajectory/Monte-Carlo approach, Aerosol Sience and Technology 30 (1999) 40-61.
49. *V.I. Vishnyakov, S.A. Kiro, M.V. Oprya, O.D. Chursina, A.A. Ennan* Numerical and experimental study of the fume chemical composition in gas metal arc welding, Aerosol Science and Engineering 2 (2018) 109-117.
50. *J. Takahashi, H. Nakashima, N. Fujii* Fume particle size distribution and fume generation rate during arc welding of cast iron, Industrial Health 58 (2020) 325-334.

Фізика аеродисперсних систем. – 2022. – № 60. – С.120-142

Вишняков В.І., Дараков Д.С., Еннан А.А. , Кіро С.А.

Виділення диму електричною дугою при газовому дуговому зварюванні

АНОТАЦІЯ

Методом чисельного моделювання досліджено вплив режиму зварювальної дуги на утворення зварювального диму шляхом опису окремих процесів в областях просторового заряду біля електродів у зварювальній дузі з плавким електродом. Моделювання включає в себе розрахунок температурних профілів для електронів і важкого компонента, розрахунок просторового розподілу густини газових компонентів, середнього вільного пробігу частинок газу, електричного потенціалу і поля, розрахунок тепловіддачі від електродного дроту (анода) до області розплаву (катода). Продемонстровано утворення високотемпературної металевої пари з ванни розплаву в навколишнє середовище як функцію струму дуги. Розглянуто зародження в плазмі зварювального диму з урахуванням іонізації атомів пари через їх взаємодію з поверхнею зародка. Розраховується зростання крапель ядра шляхом конденсації пари та коалесценції. Розраховано коагуляцію твердих первинних частинок для різних значень зварювального струму та продемонстровано вдихуваний розподіл частинок за розмірами.

Ключові слова: *зварювальна дуга, плазма, пари металу, конденсація, коагуляція*